Biomaterials Science

ROYAL SOCIETY OF CHEMISTRY

PAPER

View Article Online
View Journal | View Issue

Check for updates

Cite this: *Biomater. Sci.*, 2024, **12**, 2086

PET image-guided kidney injury theranostics enabled by a bipyramidal DNA framework†

Pinghui Li,[a] Zhidie Huang,[a] Xiaoyan Duan,[b,c] Tao Wang,[b,c] Shaowen Yang,[d,e] Dawei Jiang*[d,e] and Jianbo Li *[b,c]

Received 27th September 2023,
Accepted 14th February 2024

DOI: 10.1039/d3bm01575k

rsc.li/biomaterials-science

Understanding the pharmacokinetic profiles of nanomaterials in living organisms is essential for their application in disease treatment. Bipyramidal DNA frameworks (BDFs) are a type of DNA nanomaterial that have shown prospects in the fields of molecular imaging and therapy. To serve as a reference for disease-related studies involving the BDF, we constructed a ^{68}Ga-BDF and employed positron emission tomography (PET) imaging to establish its pharmacokinetic model in healthy mice. Our investigation revealed that the BDF was primarily eliminated from the body *via* the urinary system. Ureteral obstruction could significantly alter the metabolism of the urinary system. By utilizing the established pharmacokinetic model, we sensitively observed distinct imaging indicators in unilateral ureteral obstruction and acute kidney injury (a complication of ureteral obstruction) mouse models. Furthermore, we observed that the BDF showed therapeutic effects in an AKI model. We believe that the established pharmacokinetic model and unique renal excretion characteristics of the BDF will provide researchers with more information for studying kidney diseases.

1. Introduction

DNA nanotechnology was first introduced by Seeman in 1982 using pre-designed DNA modules (DNA linkages) to create the intended DNA nanostructures.[1] Based on the Watson–Crick principle, DNA strands can self-assemble into targeted DNA nanostructures. The development of nanotechnology has accelerated the use of DNA nanomaterials in biomedical applications, including biosensing,[2,3] drug delivery,[4–7] and *in vivo* imaging.[8–11] The use of pre-designed DNA single-strand sequences can confer DNA nanomaterials with the ability for precise modification and addressability. The functionalized modification of DNA nanomaterials with small molecules, peptides, and aptamers has been employed for the diagnosis and treatment of diseases.[12] Researchers have designed DNA nanomaterials of varying sizes and shapes, including triangles, rectangles, nanotubes, *etc.*,[13] all of which exhibit excellent biocompatibility and low biotoxicity for living organisms.[14,15]

Bipyramidal DNA frameworks (BDFs),[16] as one of these DNA nanomaterials, have already been applied in preclinical research. Song and his colleagues created a dual-modality molecular imaging probe for tumor imaging by employing Gd-DOTA (a magnetic resonance contrast agent) and DyLight 800 (a fluorescent molecule).[17] Furthermore, the BDF has also been used to repair cerebral ischemia/reperfusion injury through intrathecal injection.[18] However, there is currently no available baseline for mouse disease research. Prior to conducting diagnostic or therapeutic research, it is crucial for researchers to understand the pharmacokinetic data of the BDF in healthy mice. In our previous study, we initially explored the distribution of the BDF in healthy mice using fluorescence imaging and single-photon emission computed tomography (SPECT) imaging.[19] However, since these two imaging modalities were only employed for semi-quantitative studies, it was challenging to accurately establish a pharmacokinetic model for the BDF.[20,21] Compared to SPECT, positron emission tomography (PET) imaging has higher spatial resolution and sensitivity, allowing for precise quantitative studies.[22] In this study, we labeled a BDF using the radiometal isotope gallium-68 (half-life 67.83 min).[23] Subsequently, we quantified the distribution of the BDF in healthy mice using dynamic PET imaging and constructed a pharmacokinetic model, thereby offering a reference for the application of the BDF in disease research. Our study showed that the BDF was mainly excreted through the urinary system, which inspired us to research whether the BDF could be utilized to study kidney-

[a]*Inner Mongolia Medical University, Hohhot 010050, China*
[b]*Department of Nuclear Medicine, The Affiliated Hospital of Inner Mongolia Medical University, Hohhot 010050, China. E-mail: lijianbo_1235@msn.cn*
[c]*Inner Mongolia Key Laboratory of Molecular Imaging, Hohhot 010050, China*
[d]*Department of Nuclear Medicine, Union Hospital, Tongji Medical College, Huazhong University of Science and Technology, Wuhan 430022, China. E-mail: daweijiang@hust.edu.cn*
[e]*Hubei Province Key Laboratory of Molecular Imaging, Wuhan 430022, China*
†Electronic supplementary information (ESI) available. See DOI: https://doi.org/10.1039/d3bm01575k

related diseases. Ureteral obstruction could significantly alter the metabolism of the urinary system. Therefore, we established unilateral ureteral obstruction (UUO) and acute kidney injury (AKI) (a complication of ureteral obstruction) models to validate the practicality of our pharmacokinetic model.[24,25] Using the established pharmacokinetic model as a baseline, we sensitively observed alterations in the distribution of the ^{68}Ga-BDF among kidneys in UUO and AKI models. In particular, in the UUO model, the ureteral obstruction prolonged the half-life of the ^{68}Ga-BDF in the liver by approximately 3 min, indicating that more ^{68}Ga-BDF was excreted from the body through hepatic metabolism. The dynamic metabolism of the ^{68}Ga-BDF in AKI and UUO was significantly altered compared to that in healthy mice.

The bases of DNA are reductive. Point mutation in human DNA due to stimulation by reactive oxygen species (ROS) is a mechanism for cellular carcinogenesis.[26] This indicates that the bases of DNA can undergo redox reactions with ROS. ROS are involved in the pathogenesis of AKI,[27] which inspired us to utilize the BDF for the treatment of AKI and assess prognosis using the established pharmacokinetic model. Excitingly, after treatment with the BDF, the time-activity curves (TACs) of the kidneys in the AKI model were close to those of healthy mice, and blood creatinine and urea nitrogen levels were alleviated.

We used the pharmacokinetic model as a baseline for studying AKI by conducting prognosis assessments. The characteristics of renal metabolism would suggest that the BDF has more potential for application in renal diseases. The pharmacokinetic model will provide researchers with a reference for the disease applications of the BDF.

2. Experimental section

2.1 General

DNA oligonucleotides (including Cy5-A20) were purchased from Sangon Biotech (Shanghai) Co., Ltd (China). NOTA-A20 was purchased from Suzhou Biosyntech Co., Ltd (China). The cell culture medium was purchased from GIBCO (Grand Island, NY, USA). Chemical reagents were purchased from Beijing Solarbio Science & Technology Co., Ltd (China) and used as received, unless stated otherwise.

2.2 Preparation and purification of the BDF

The preparation method of the BDF has been reported in the previous literature published by our group. In brief, the BDF was prepared by annealing six DNA oligonucleotide strands (the oligonucleotide sequences are shown in the ESI, Table S1†) in TM buffer (10 mM Tris-base, 50 mM $MgCl_2$, pH 8.0) and rapidly cooling them from 95 °C to 4 °C within 30 min to obtain the BDF. The BDF was purified by 1.5% agarose gel electrophoresis (running buffer: 1× TAE containing 12.5 mM $MgAc_2$), which was run at 4 °C for 20 min.

2.3 Polyacrylamide gel electrophoresis

Polyacrylamide gel electrophoresis (PAGE) was used to characterize the self-assembly process of the BDF. DNA samples were separated on 8% PAGE gels (running buffer: 1× TAE with 12.5 mM $MgAc_2$) and run for 90 min at 4 °C. The gels were then stained with GelRed and imaged under an imaging system (UVP GelStudio PLUS Touch, Germany).

2.4 Hydrodynamic radius

A dynamic light scattering instrument (DLS, Nano Series, Malvern Instruments) was used to characterize the particle size of the BDF. 1.5 mL (50 μM) of BDF solution was taken for the assay and five cycles of measurements were performed, each cycle lasting for 1 min.

2.5 *In vitro* stability of the BDF

The BDF was mixed with 100% mouse serum or 100% fetal bovine serum or 1× PBS buffer, respectively, at a volume ratio of 1 : 10 and allowed to stand for 24 h at 37 °C. The stability of the BDF was examined using 2% agarose gel (running buffer: TAE-Mg^{2+} buffer). Images were analyzed using Image J.

2.6 Cytotoxicity assay of the BDF

The cytotoxicity of the BDF was detected using Cell Counting Kit-8 (CCK-8). HEK293 cells were cultured in Duchenne's Modified Eagle's Medium (DMEM) supplemented with 10% fetal bovine serum (FBS). The cells were stored in a humidified incubator at 37 °C with 5% CO_2. After seeding 5000 cells per well in a 96-well plate and culturing them overnight, 10 μL of a certain concentration of the BDF was added to each well and incubated for 24 h at 37 °C. Then, 10 μL of CCK-8 solution was added to each well and incubated at 37 °C for 4 h. Absorbance values were measured at 450 nm using a microplate reader (Biotek Epoch, USA).

2.7 Radiolabeling of the BDF

10 μL of NOTA-A20 (3 nmol) was added to 300 μL, 74 MBq (2 mCi) of $^{68}GaCl_3$ (NaOAc buffer, 0.1 M, pH 7.5) at 37 °C and reacted for 30 min with continuous shaking. The reaction was monitored in real time using radio thin layer chromatography (radio-TLC). The reaction mixture was purified using a PD-10 column to obtain ^{68}Ga-A20, which was then mixed and hybridized with the BDF (the BDF has three T20 side chains, and the preparation method is detailed in section 2.2. The molar ratio of ^{68}Ga-A20/BDF is 3 : 1 in PBS buffer, pH 7.0), resulting in the ^{68}Ga-BDF.

2.8 Dynamic PET imaging of the ^{68}Ga-BDF in healthy mice

The study protocol was approved by the Medical Ethics Committee of Inner Mongolia Medical University (no. YKD202001143). The animal experiments were performed in accordance with the 'Guide for the Care and Use of Laboratory Animals' (Institute of Laboratory Animal Resources, Commission on Life Sciences, National Research Council, ISBN: 0-309-58869-3, 140 pages, 1996). Mice were maintained

under specific pathogen-free conditions with a light–dark cycle of 12 h, a temperature of 22 ± 2 °C, and a humidity of 45 ± 10%.

BALB/c mice (6–8 weeks, 17–20 g, Beijing Vital River Laboratory Animal Technology Co., Ltd.) were injected with 1.85 MBq (50 μCi) of the ^{68}Ga-BDF through the tail vein. Mice were anesthetized by inhalation of an isoflurane–air mixture (V : V = 2%–3%) and subjected to dynamic PET imaging for 60 min to monitor the distribution of the ^{68}Ga-BDF *in vivo*. PET scans were performed with a micro-PET/CT scanner (Inveon MM, Siemens Ltd, Munich, Germany). The histogram file was reframed with a total of 20 frames: 60 s × 10 frames and 300 s × 10 frames. PET data were reconstructed using an ordered subsets expectation maximization 3D or maximum *a posteriori* (OSEM3D/MAP) algorithm.

2.9 Construction of the pharmacokinetic model

To establish the time-activity curve (TAC) for the region of interest (ROI), uptake values were expressed as a percentage of injected dose per gram of tissue (%ID g^{-1}). The circulation half-life was obtained by fitting the blood pool time–activity curve with a biexponential model.

The distribution and clearance of the ^{68}Ga-BDF in major organs were investigated by analyzing the ROI data. Equation curves were derived from the ROI data of the heart, kidneys, bladder and liver using the Graphpad curve fitting tool, and their upper and lower limits and standard deviations were calculated. The half-life of the ^{68}Ga-BDF in each major organ was calculated using the equation curve. The accuracy of these rate constants was important for BDF metabolism.

2.10 Dynamic PET imaging of the ^{68}Ga-BDF in the UUO model

The UUO model was constructed by ligating the left ureter in mice. An entire ureteral obstruction was achieved in mice under general anesthesia by double-ligating the left ureter with 4–0 silk following exposure by a flack incision. After surgery, all models were fed and watered normally under standard environmental conditions. Dynamic PET imaging and image processing of the ^{68}Ga-BDF in the UUO model mice were performed by following the same procedures as those for the ^{68}Ga-BDF in healthy mice, as described in the section of "Dynamic PET imaging of the ^{68}Ga-BDF in healthy mice".

2.11 Construction, treatment, and PET imaging of the AKI model

The AKI model was constructed by intramuscular injection of 50% glycerol after 15 h of water fasting. Dynamic PET imaging of the AKI model was performed at 2 and 24 h after glycerol injection. Dynamic PET imaging and image processing of the ^{68}Ga-BDF in the AKI model were performed by following the same procedures as those for the ^{68}Ga-BDF in healthy mice, as described in the section of "Dynamic PET imaging of the ^{68}Ga-BDF in healthy mice".

The therapeutic effect of the BDF on acute kidney injury was observed by intravenous injection of the BDF (0.5 mg kg^{-1}) 2 h after modeling of the AKI model. The therapeutic effect was evaluated using dynamic PET imaging with the ^{68}Ga-BDF. A control experiment was also performed in which the AKI model was injected with PBS through the tail vein.

At the end of 24 hours of PET imaging, the blood and kidneys were collected from the experimental mice. The serum was centrifuged at 3000*g* for 5 min, and the supernatant was collected and assayed for plasma creatinine and urea nitrogen levels. Urea nitrogen levels were measured using a blood urea nitrogen enzymatic kit and creatinine levels were measured using the QuantiChrom creatinine assay kit. Both kits were purchased from Rayto Life and Analytical Sciences Co., Ltd (Shenzhen, China).

2.12 Histological analysis of the major organs

The major organs or tissues in healthy mice, and those in UUO and AKI mouse models were collected after PET imaging. Tissue samples were fixed with 4% paraformaldehyde, dehydrated stepwise, embedded in paraffin and cut into 4 μm thick slices. These slices were then stained with hematoxylin and eosin (H&E).

2.13 Fluorescence imaging of the isolated kidneys from experimental mice

The Cy5-BDF was prepared using the same procedure as the preparation of the ^{68}Ga-BDF, and hybridized by mixing the BDF with Cy5-A20 in PBS buffer (pH 7.0) according to a molar ratio of 1 : 3. The Cy5-BDF was injected into the AKI model or healthy mice *via* the tail vein, and the kidneys were removed after the mice were euthanized at different time points, and their fluorescence imaging was performed on a small-animal *in vivo* optical imaging platform (PerkinElmer IVIS Lumina III, USA). After imaging, the kidneys were fixed in 4% paraformaldehyde, dehydrated stepwise, paraffin-embedded, and sliced, and then the fluorescence signals were detected under a fluorescence microscope (Pannoramic MIDI, Budapest, Hungary).

2.14 *In vitro* evaluation of the antioxidant effects of the BDF

CCK-8 assay was used to test the antioxidant effects of the BDF. HEK293 cells were cultured in DMEM supplemented with 10% FBS. The cells were stored in a humidified incubator at 37 °C with 5% CO_2. After seeding 5000 cells per well in a 96-well plate and culturing them overnight, H_2O_2 (5 mM) or a mixture of the BDF (10 μM) and H_2O_2 (5 mM) was added to each well and incubated at 37 °C for 24 h. Afterwards, 10 μL of CCK-8 solution was added to each well and incubated at 37 °C for 4 h. Absorbance values were measured at 450 nm using a microplate reader (Biotek Epoch, America).

2.15 Intracellular MDA (malondialdehyde) levels

HEK293 cells were seeded into 10 mL sterile culture dishes at a density of 106 cells per ml. Each dish was then incubated with 5 mM H_2O_2 or a mixture of 10 μM BDF and 5 mM H_2O_2 for 24 hours at 37 °C. Cell clusters were obtained by centrifuging the cell-containing medium at 1000 rpm for 4 min. MDA

was detected using a commercially available MDA assay kit (Jiancheng Bioengineering, Nanjing, China).

2.16 Hemolysis assay

The toxicity of the BDF on cells was tested at 10, 50, and 100 μM at 37 °C for one hour. H_2O was used as the positive control for hemolysis and PBS as negative control. After one hour, the plate was centrifuged at 13 000*g* for 10 min and 100 μL of supernatant per well was transferred to a new 96-well plate. Absorbance values were measured at 540 nm using a microplate reader (Biotek Epoch, USA). The data were calculated according to the standard formula:

$$\%\ \text{Hemolysis} = ([A_{540} - {}_{\min}A_{540}]/[{}_{\max}A_{540} - {}_{\min}A_{540}]) \times 100\%$$

where A_{540} is the average absorption of the compound at 540 nm; ${}_{\min}A_{540}$ is the average absorption of PBS; ${}_{\max}A_{540}$ is the average absorption of H_2O.

2.17 Statistical analysis

Quantitative data were expressed as mean and standard deviation. Statistical analysis was performed using the Student's *t*-test. $p < 0.05$ was considered statistically significant.

3. Results and discussion

3.1 Preparation and characterization of the BDF

The BDF was successfully prepared using a one-step annealing method by dissolving the six oligonucleotide single strands with designed sequences in equal proportions in TM buffer, as shown in Fig. 1A. The sequence information of the six oligonucleotide single strands for assembling the BDF is shown in the ESI.†

The assembly process of the BDF was characterized using PAGE (Fig. 1B) and as the oligonucleotide single chains were added one by one, the position of the formed structure in the lane was closer to the starting point, indicating that the molecular weight of the formed structure gradually became larger, until all six oligonucleotide single chains were added to form the target BDF product. DLS analysis showed that the average diameter of the BDF was 26.91 ± 2.45 nm (Fig. S1†). We have previously observed the structure of the BDF through atomic force microscopy (AFM) and measured the length of the structure to be around ~14 nm.[19] Renal accumulation of relatively small nanoparticles, with diameters between 5 and 8 nm, was found to be 1.7 times higher than the accumulation of 20–50 nm nanoparticles.[28] Therefore, the BDF could effectively accumulate in the kidneys.

3.2 *In vitro* stability and cytotoxicity studies of the BDF

In order to subsequently study the distribution and metabolism of the BDF *in vivo*, an *in vitro* stability study of the BDF was carried out by co-incubating the BDF with 100% mouse serum, 100% fetal bovine serum or 1× PBS buffer for a certain period of time, respectively. The results showed that about 70% of the BDF could maintain its intact structure in mouse serum and FBS at 4 h (Fig. 2A & B).

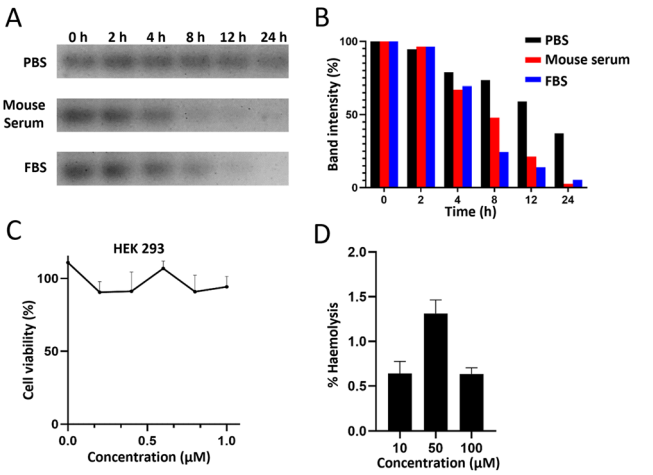

Fig. 2 *In vitro* stability and cytotoxicity studies of the BDF. (A) Evaluation of the stability of the BDF in PBS, mouse serum and fetal bovine serum using 2% agarose gel. (B) Quantification of Fig. 2A. (C) Cytotoxicity of the BDF in HEK293 cells was detected using the CCK-8 assay. (D) The hemolysis rates at different concentrations of the BDF.

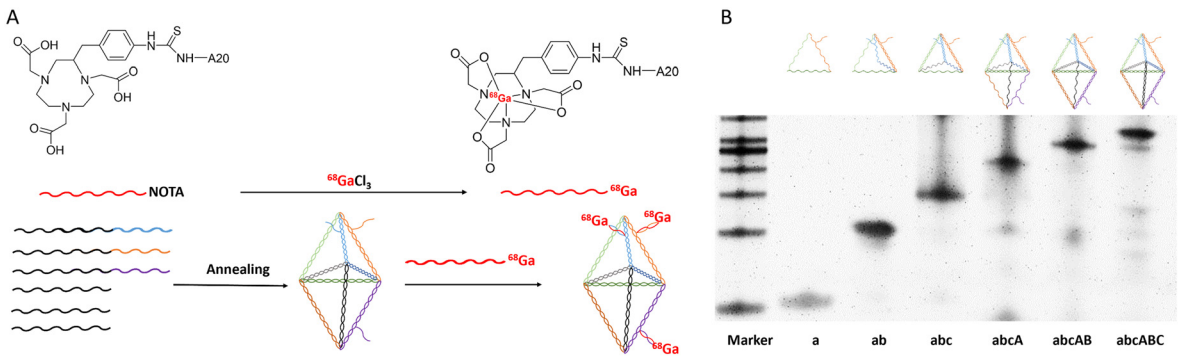

Fig. 1 Schematic illustration and characterization of the self-assembly of the bipyramidal DNA framework. (A) Scheme of the assembly and radiolabelling process of the BDF using ^{68}Ga. (B) Polyacrylamide gel electrophoresis (PAGE) characterizes the self-assembly process of the BDF.

The cytotoxicity of the BDF was detected using CCK-8 assay. HEK293 cells were incubated with different concentrations of the BDF for 24 h. The results showed that 0.2 μM to 1.0 μM BDF had little effect on cell viability, which indicated that the BDF was a safe nanomaterial and provided biosafety for subsequent experiments (Fig. 2C). The BDF was assessed for its toxicity towards red blood cells and was shown to be nonhemolytic, even at high concentrations of 100 μM (Fig. 2D). Hemolysis was not considered for % haemolysis of less than 5%.

3.3 Radiolabeling of the BDF

The process of labeling the BDF with the positron-emitting nuclide ^{68}Ga was divided into two steps, as shown in Fig. 1A. ^{68}Ga-A20 was prepared by ^{68}Ga labeling of NOTA-A20 and purified by PD-10 columns, with the radiochemical purity being 95%. The specific activity of ^{68}Ga-A20 was in the range of 18.5–22.2 MBq nmol^{-1} (500–600 μCi nmol^{-1}). The BDF prepared in this study carried three oligonucleotide chains (T20) on its side arm. Using the complementary pairing of adenine (A) and thymine (T), the PET probe ^{68}Ga-BDF was prepared by hybridizing the BDF with ^{68}Ga-A20 in a molar ratio of 1 : 3 at room temperature.

3.4 Establishment of a pharmacokinetic model for the BDF in healthy mice

Understanding the pharmacokinetic profiles of nanomaterials in living organisms is essential for their application in disease treatment. To establish a pharmacokinetic model of the BDF in healthy mice, ~1.85 MBq (50 μCi) of the ^{68}Ga-BDF was injected into healthy mice *via* the tail vein under anesthesia, while dynamic PET imaging was performed for 60 min. The distribution and metabolic pathways of the ^{68}Ga-BDF *in vivo* were monitored in real time and non-invasively by PET imaging. As shown in Fig. 3A, the signal was promptly detected in the blood pool after the injection of the ^{68}Ga-BDF. After 1 min, the ^{68}Ga-BDF began to accumulate in the kidneys, reaching its peak uptake value at 5 minutes. Subsequently, it

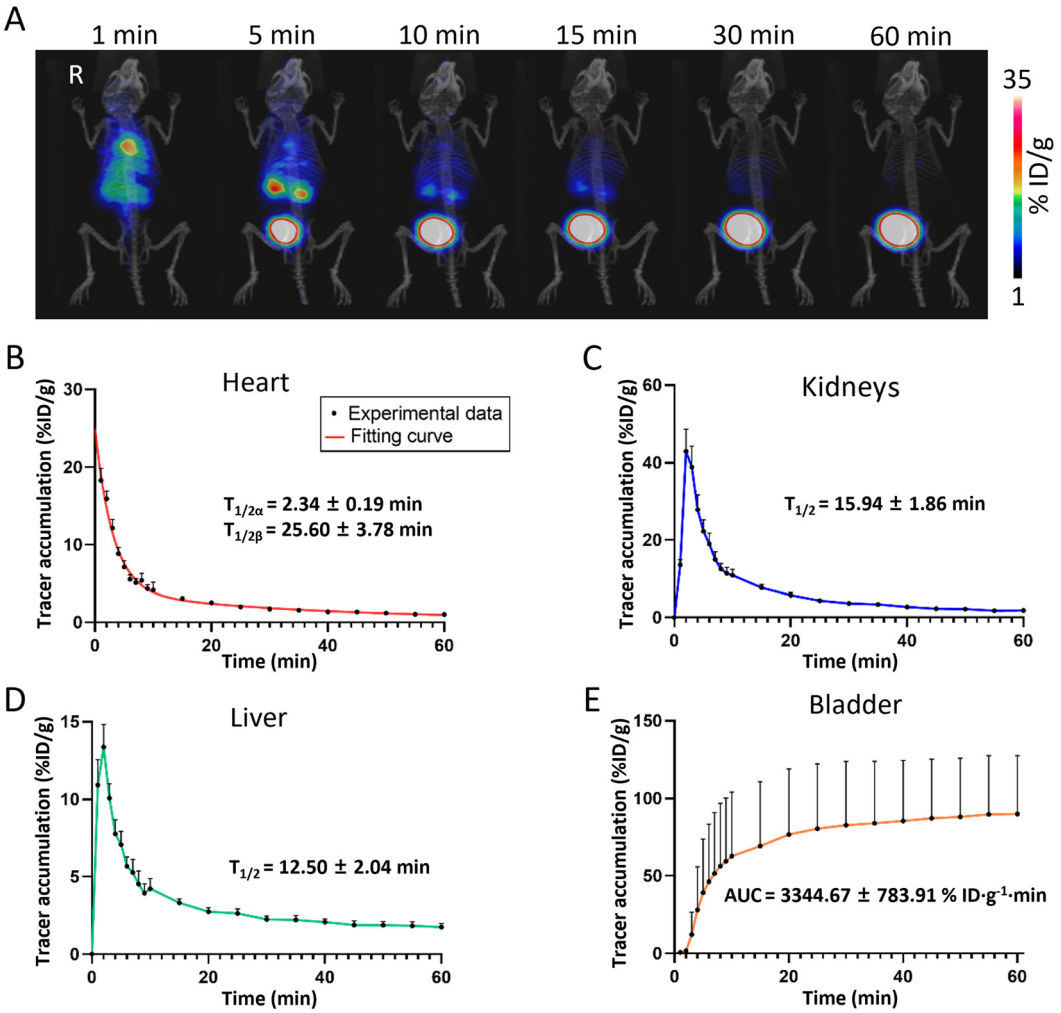

Fig. 3 Dynamic PET images and time–activity curves (TACs) of major organs. (A) Dynamic PET images of healthy mice after intravenous injection of the ^{68}Ga-BDF (n = 3). (B–E) TAC and the half-life of the ^{68}Ga-BDF in major organs (heart, kidneys, liver and bladder, respectively).

accumulated in the bladder *via* the ureter. The imaging results revealed that the ^{68}Ga-BDF primarily underwent metabolism *via* the urinary system. In addition to renal metabolism, a portion of the ^{68}Ga-BDF was metabolized in the liver. The results indicated that in healthy mice, the kidneys and liver were the main organs for BDF metabolism. This was consistent with our previous study in which the ^{99m}Tc-BDF and DyLight 755-BDF were metabolized mainly through the kidneys and liver.

The uptake value of the ^{68}Ga-BDF in each major organ was quantified by ROI analysis. A two-compartment fitting model was used to determine the half-life of the ^{68}Ga-BDF in blood. The circulating half-life of the ^{68}Ga-BDF in blood was 2.34 ± 0.19 min and 25.60 ± 3.78 min, respectively (Fig. 3B). To assess renal function, we obtained data using time–activity curves (TACs) of the kidneys. A single-compartment fitting model was used to determine the half-life of the ^{68}Ga-BDF in the kidneys and liver. The half-life times of the ^{68}Ga-BDF in the kidneys and liver were 15.94 ± 1.86 min and 12.50 ± 2.04 min, respectively (Fig. 3C & D). The accumulation data in the bladder were used as a clearance index and the area under the curve (AUC) of the ^{68}Ga-BDF in the bladder was measured, with a value of 3344.67 ± 783.91% ID g^{-1} min (Fig. 3E). This indicated that the BDF could be excreted efficiently out of the body. By obtaining the distribution of the BDF in healthy mice, it was possible to provide a reference standard for the distribution of the BDF in different disease models.

3.5 Toxicological study of the ^{68}Ga-BDF

After studying the distribution and metabolism of the ^{68}Ga-BDF in healthy mice, the mice were euthanized after PET imaging and the major organs were removed for pathological analysis. A control group was set up by administering an equal volume of PBS. The results of H&E staining showed that there were no obvious pathological changes in the heart, liver, spleen, kidneys and lungs of healthy mice injected with the ^{68}Ga-BDF, compared with the control group, as shown in Fig. S2.†

3.6 Studying UUO and AKI using the established pharmacokinetic model

The distribution and metabolic information of the ^{68}Ga-BDF in healthy mice had been determined, and a pharmacokinetic model in healthy mice had been established. The results of the study showed that the ^{68}Ga-BDF was primarily excreted from the body *via* the urinary system. In kidney-related diseases, ureteral obstruction could significantly alter the metabolism of the urinary system. To validate the reliability of our pharmacokinetic model, we further explored the potential application of the ^{68}Ga-BDF in the UUO model.

The UUO model was established by ligating the left ureter of the mouse. A 60-minute dynamic PET imaging was performed on the UUO model 24 hours after surgery. As shown in the top row of Fig. 4A, the radioactive signal was detected in the blood pool immediately after injection of the ^{68}Ga-BDF. The signal of the ^{68}Ga-BDF in the healthy (right) kidney exhibited initial strengthening followed by subsequent weakening within 60 minutes. These findings were consistent with the distribution and metabolism of the ^{68}Ga-BDF observed in healthy mice. In contrast, the ^{68}Ga-BDF continuously accumulated in the obstructed (left) kidney during the 60-minute dynamic PET imaging. The uptake values of the ^{68}Ga-BDF in the major organs of the UUO model were also quantified by ROI analysis. The half-life of the ^{68}Ga-BDF in the blood or kidneys was also determined using two-compartment or one-compartment fitting models. The blood circulatory half-life of the ^{68}Ga-BDF in the UUO model, 2.74 ± 0.22 and 46.24 ± 15.79 min, was prolonged by about 21 min compared with that of healthy mice (Fig. 4B & 3B). There were significant differences in the uptake and distribution of the ^{68}Ga-BDF between the obstructed kidney and the healthy kidney. Renal TAC results in the UUO model showed continuous accumulation of the ^{68}Ga-BDF in the obstructed kidney compared to the contralateral healthy kidney (Fig. 4C). The longer exclusion time of the ^{68}Ga-BDF in the obstructed kidney indicated damage to that kidney. The metabolic trend of the ^{68}Ga-BDF in the contralateral healthy kidney of the UUO model was consistent with that in the kidney of healthy mice, with a half-life of 11.49 ± 1.06 min. The uptake of the ^{68}Ga-BDF in the bladder was slowed down due to renal injury on one side in the UUO model (Fig. S3a† & Fig. 3E), suggesting that the overall excretion efficiency of the ^{68}Ga-BDF was reduced in the UUO model. The circulating half-life of the ^{68}Ga-BDF was longer in the UUO model compared with that in healthy mice. In addition, the half-life of the ^{68}Ga-BDF in the liver was prolonged by approximately 3 min (Fig. S3b† & Fig. 3D), suggesting that more BDF was metabolized by the liver after unilateral renal obstruction. The experimental results showed that the half-life of the ^{68}Ga-BDF was changed in all the major organs of the UUO model. H&E staining showed that UUO resulted in marked renal tubular epithelial cell necrosis, tubular atrophy, and vacuolization (Fig. S4†).

AKI is a complication of ureteral obstruction, characterized by the rapid loss of renal excretory function.[29] Clinically, the diagnosis is based on the accumulation of a number of end products (urea nitrogen and creatinine) in the blood.[30] Therefore, based on the ability of the ^{68}Ga-BDF to effectively diagnose metabolic abnormalities in the obstructed kidney in the UUO model, we wanted to further explore the role of the ^{68}Ga-BDF in AKI. As shown in the bottom row of Fig. 4A, we performed dynamic imaging of the ^{68}Ga-BDF in the AKI model. Compared with the imaging results of both kidneys in healthy mice, both kidneys of the AKI model showed radioactive signals at all time points, and until 60 min, there were still significant radioactive signals from both kidneys. The renal uptake values of the ^{68}Ga-BDF in the AKI model were also quantified by ROI analysis. The renal TAC in the AKI model showed a relatively stable trend after 10 min, which was significantly different from that in healthy mice (Fig. 4D & 3C).

In previously published imaging studies, ^{99m}Tc-DTPA was used to study the imaging characteristics of different stages of ureteral obstruction in rabbits, and renal contrast-enhanced

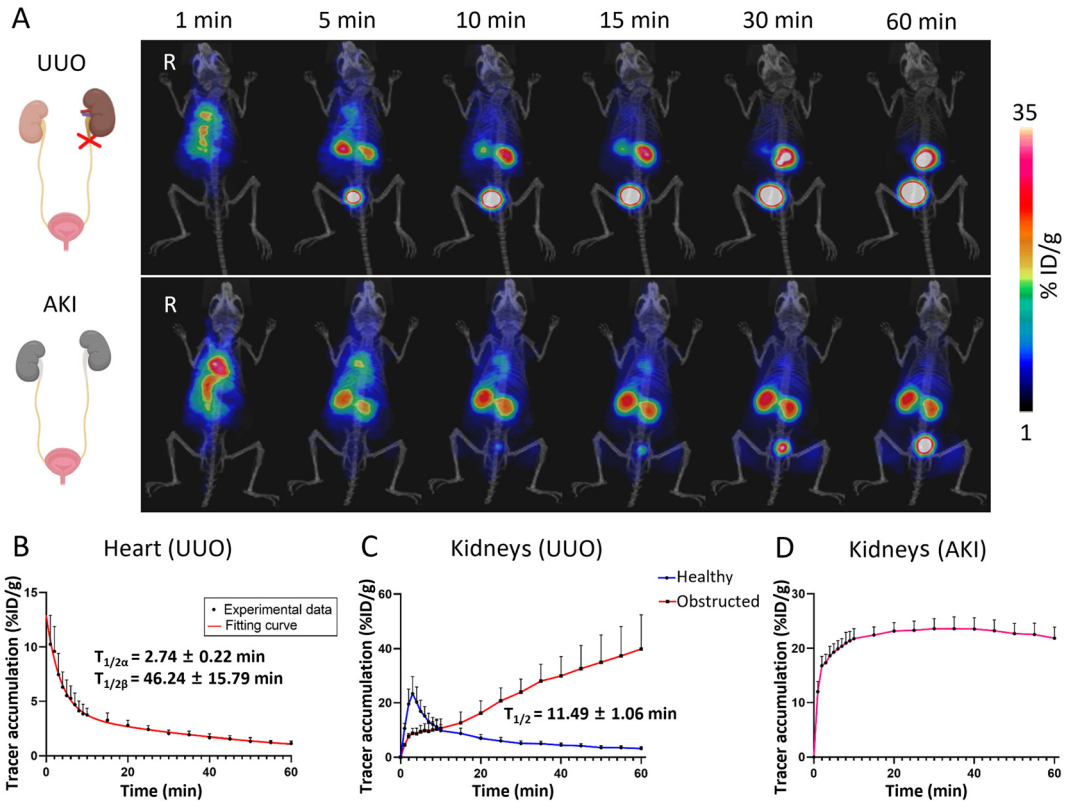

Fig. 4 Dynamic PET images and TACs of major organs. (A) Dynamic PET images of different models (UUO and AKI) after intravenous injection of the ^{68}Ga-BDF (n = 3). (B) TAC and the half-life of the ^{68}Ga-BDF in the heart of the UUO model. (C) TAC of the ^{68}Ga-BDF in the kidneys of the UUO model. (D) TAC of the ^{68}Ga-BDF in the kidneys of the AKI model.

ultrasonography (CEUS) and multiparametric MRI were used to assess acute kidney injury.[31,32] Compared to these studies, PET demonstrates a more precise quantitative advantage. Based on the distribution and metabolism of the ^{68}Ga-BDF in healthy mice, it is a reference for the diagnosis of UUO and AKI models. Therefore, before exploring the metabolic information of the BDF under pathological conditions, it is important to first determine its distribution and metabolism under healthy conditions.

3.7 The BDF effectively improves renal function in the AKI model

The essence of the BDF is DNA. DNA undergoes point mutation as a result of stimulation by reactive oxygen species (mainly H_2O_2 and $^{\bullet}OH$), which is a mechanism that leads to cellular carcinogenesis.[33] The bases of DNA, especially guanine, can undergo redox reactions with $^{\bullet}OH$. Its oxidative product, 7,8-dihydro-8-oxoguanine (8-oxoG), is the most common product of oxidative damage among all bases and is considered a biomarker of oxidative stress.[34,35] ROS are involved in the pathological conditions of AKI, and excess ROS within the renal parenchyma lead to mitochondrial swelling, inducing cell apoptosis and necrosis.[36] The BDF consumes a portion of ROS, protecting more cells from damage, which indicates that it can be used in redox reactions with $^{\bullet}OH$ in the kidneys to mitigate AKI. We designed an experiment (Fig. 5A) to further investigate the use of the BDF in AKI. A separate control group was set up and an equal amount of PBS was given. The administration of the BDF was approximately 10.9 μg per mouse. The increase of creatinine and urea nitrogen levels in plasma at a 2-hour time point confirmed the success of the modeling (p < 0.0001) (Fig. S5†). Dynamic imaging was performed 24 hours after BDF or PBS injection (Fig. 5B). The signal accumulation of the ^{68}Ga-BDF in the kidneys was significantly increased and the excretion rate was accelerated after BDF treatment compared to that in the control group. Excitingly, the TAC of the heart well (blood pool) and kidney in the BDF-treated group was closer to that of healthy mice (Fig. 5C & D), and the therapeutic effect was also observed at the intramuscular injection site. The signal at the injection site showed a decreasing trend after 20 min after BDF treatment. Compared to the PBS treatment group, the activity signal continued to accumulate (Fig. 5E). The prognostic assessment of AKI benefited from the established pharmacokinetic model.

The fluorescence imaging of the kidneys (Fig. 6A) and the results of renal sections (Fig. 6B) showed that the BDF was retained in the damaged kidneys, which provided a prerequisite for the treatment of AKI with the BDF. Serum creatinine and urea nitrogen levels were significantly decreased in the

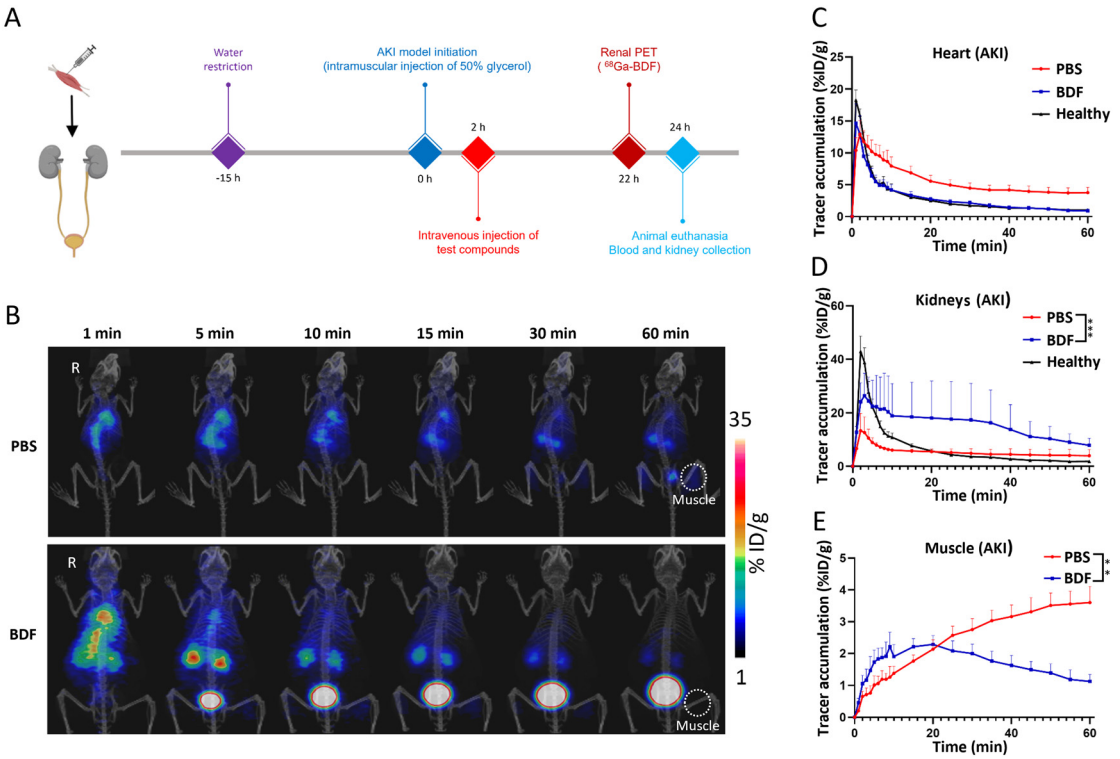

Fig. 5 Treatment of AKI with PBS or the BDF. (A) Time schedule of the AKI model establishment, treatment, and PET imaging using the ^{68}Ga-BDF. (B) Dynamic PET images of AKI mice after treatment with PBS or the BDF. The white circles represent the injection sites of glycerol. (C–E) TAC of the ^{68}Ga-BDF in major organs (heart, kidneys and muscle, respectively) of AKI mice after treatment with PBS or the BDF.

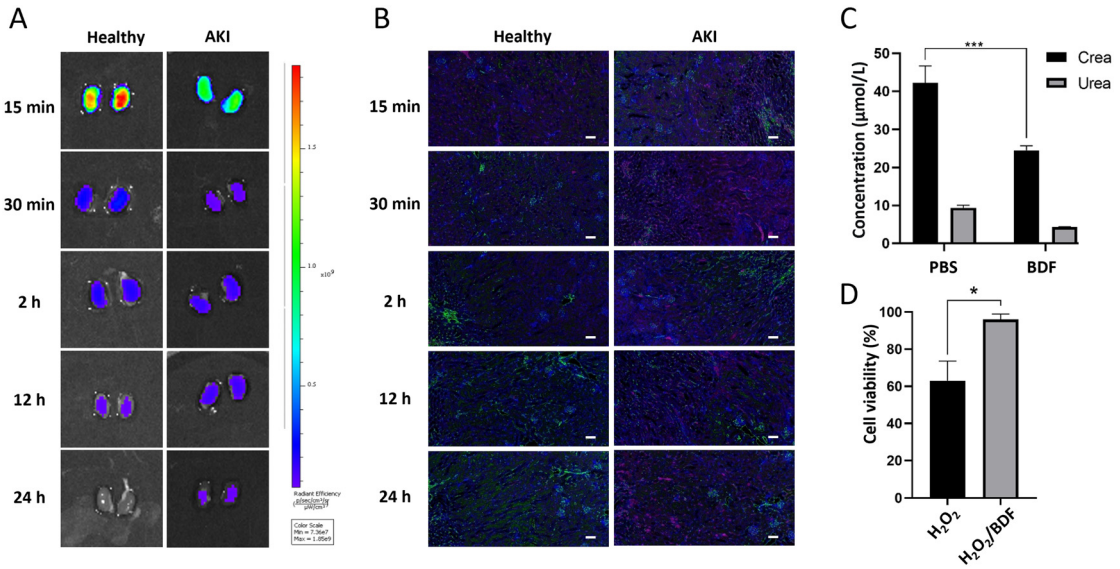

Fig. 6 (A and B) Fluorescence images and sections of the kidneys in healthy and AKI mice at different time points after intravenous injection of the Cy5-BDF. Pink represents the Cy5-BDF, green represents the blood vessels, and blue represents nucleic acid. Scale bar = 50 μm. (C) Serum creatinine and urea nitrogen levels in plasma after treatment with PBS or the BDF ($p < 0.001$). (D) Viability of cells incubated in H_2O_2/BDF or H_2O_2 for 24 hours ($p < 0.05$).

BDF-treated group (Fig. 6C). Pathological sections showed that vacuolization of tubular epithelial cells was alleviated after BDF treatment (Fig. S6†).

To verify the reductive properties of the BDF, HEK293 cells were used to investigate whether the BDF could alleviate the deleterious effects of ROS on cellular function. The CCK8

experiment proved that the BDF alleviated the oxidative damage on cells caused by H_2O_2 ($p < 0.05$) (Fig. 6D). MDA was the end-product of lipid peroxidation in cell membranes and could be used to assess cell membrane damage.[37] To assess the level of oxidative stress in cells, the MDA content in cell clusters was measured. The treatment using the BDF led to a decrease in MDA content compared to the control group, demonstrating that the cells suffered less oxidative damage (Fig. S7†). Compared to other nanomaterials used for treating AKI, such as metal compound nanomaterials (POMs, TPNs), the advantage of DNA nanomaterials lies in their inherent biocompatibility and low biotoxicity.[38–40] Therefore, the BDF with reducing properties could exert antioxidant effects. In the AKI model, the established pharmacokinetic model could not only lead to rapid diagnosis but also assess the therapeutic effects of the BDF.

4. Conclusions

BDFs, as a DNA nanomaterial, have been used in preclinical experiments and achieved remarkable results in imaging and therapy. In this study, we designed a simple and efficient method for a gallium-68-labeled BDF. Through dynamic PET imaging, the distribution metabolism of the ^{68}Ga-BDF in mice was quantified, which could provide valuable information for the study of the ^{68}Ga-BDF in disease models. This research indicated that the ^{68}Ga-BDF had a short half-life in blood and was rapidly cleared through the kidneys, with only a small portion cleared through the liver. Based on the distribution of the ^{68}Ga-BDF in healthy mice, we further investigated the distribution and metabolism of the ^{68}Ga-BDF in UUO and AKI models. Compared to healthy mice, we observed a significant change in the clearance pattern of the ^{68}Ga-BDF in both UUO and AKI. Our research results will provide a reference for the application of DNA nanomaterial probes in the medical field. In future studies, we will explore the potential of the BDF as a drug carrier. We believe that the establishment of the BDF pharmacokinetic model can provide valuable information for the study of the BDF *in vivo* in animals.

Conflicts of interest

There are no conflicts to declare.

Acknowledgements

This work was supported by the National Natural Science Foundation of China (No. 82060324), the "Youth Science and Technology Talents in Colleges and Universities" Support Program Project of the Inner Mongolia Education Department (NJYT22016), the "Postgraduate Talent Excellence Program" Support Program Project of Inner Mongolia Medical University (YKD2023ZY001) and the "Inner Mongolia Autonomous Region master postgraduate research innovation project" Support Program Project of Inner Mongolia Education Department (S20231183Z).

References

1 N. C. Seeman, *J. Theor. Biol.*, 1982, **99**, 237–247.
2 D. Ye, X. Zuo and C. Fan, *Annu. Rev. Anal. Chem.*, 2018, **11**, 171–195.
3 J. Liu, L. Yan, S. He and J. Hu, *Nano Res.*, 2022, **15**, 3504–3513.
4 T. Kim, K. Nam, Y. M. Kim, K. Yang and Y. H. Roh, *ACS Nano*, 2021, **15**, 1942–1951.
5 Q. Hu, H. Li, L. Wang, H. Gu and C. Fan, *Chem. Rev.*, 2019, **119**, 6459–6506.
6 A. Kumar, A. Ahmad, M. M. Ansari, V. Gowd, S. Rashid, A. A. Chaudhary, H. A. Rudayni, S. A. Alsalamah and R. Khan, *Semin. Cancer Biol.*, 2022, **86**, 54–68.
7 Z. Ge, L. Guo, G. Wu, J. Li, Y. Sun, Y. Hou, J. Shi, S. Song, L. Wang, C. Fan, H. Lu and Q. Li, *Small*, 2020, **16**, e1904857.
8 D. Jiang, Y. Sun, J. Li, Q. Li, M. Lv, B. Zhu, T. Tian, D. Cheng, J. Xia, L. Zhang, L. Wang, Q. Huang, J. Shi and C. Fan, *ACS Appl. Mater. Interfaces*, 2016, **8**, 4378–4384.
9 Y. Zeng, R. L. Nixon, W. Liu and R. Wang, *Biomaterials*, 2021, **268**, 120560.
10 F. Li, J. Li, B. Dong, F. Wang, C. Fan and X. Zuo, *Chem. Soc. Rev.*, 2021, **50**, 5650–5667.
11 D. Jiang, C. G. England and W. Cai, *J. Controlled Release*, 2016, **239**, 27–38.
12 W. Ma, Y. Zhan, Y. Zhang, C. Mao, X. Xie and Y. Lin, *Signal Transduction Targeted Ther.*, 2021, **6**, 351.
13 H. Wang, Q. Liu, X. Lan and D. Jiang, *Angew. Chem., Int. Ed.*, 2022, **61**, e202111980.
14 J. Yan, X. Zhan, Z. Zhang, K. Chen, M. Wang, Y. Sun, B. He and Y. Liang, *J. Nanobiotechnol.*, 2021, **19**, 412.
15 D. Jiang, Z. Ge, H.-J. Im, C. G. England, D. Ni, J. Hou, L. Zhang, C. J. Kutyreff, Y. Yan, Y. Liu, S. Y. Cho, J. W. Engle, J. Shi, P. Huang, C. Fan, H. Yan and W. Cai, *Nat. Biomed. Eng.*, 2018, **2**, 865–877.
16 C. M. Erben, R. P. Goodman and A. J. Turberfield, *J. Am. Chem. Soc.*, 2007, **129**, 6992–6993.
17 L. Song, Z. Wang, J. Liu, T. Wang, Q. Jiang and B. Ding, *ACS Appl. Bio Mater.*, 2020, **3**, 2854–2860.
18 S. Li, D. Jiang, Z. T. Rosenkrans, T. E. Barnhart, E. B. Ehlerding, D. Ni, J. W. Engle and W. Cai, *Nano Lett.*, 2019, **19**, 7334–7341.
19 J. Li, D. Jiang, B. Bao, Y. He, L. Liu and X. Wang, *Bioconjugate Chem.*, 2016, **27**, 905–910.
20 B. L. Holman and S. S. Tumeh, *J. Am. Med. Assoc.*, 1990, **263**, 561–564.
21 H. Kang, M.-W. Kang, S. Kashiwagi and H. S. Choi, *J Immunother. Cancer*, 2022, **10**, e004936.
22 G. Muehllehner and J. S. Karp, *Phys. Med. Biol.*, 2006, **51**, R117–R137.

23 C. Morgat, E. Hindié, A. K. Mishra, M. Allard and P. Fernandez, *Cancer Biother. Radiopharm.*, 2013, **28**, 85–97.
24 E. H. Lee, S.-H. Kim, J.-H. Shin, S. B. Park, B. H. Chi and J. H. Hwang, *BMJ Open*, 2019, **9**, e030438.
25 R. L. Chevalier, M. S. Forbes and B. A. Thornhill, *Kidney Int.*, 2009, **75**, 1145–1152.
26 E. C. Cheung and K. H. Vousden, *Nat. Rev. Cancer*, 2022, **22**, 280–297.
27 K. A. Nath and S. M. Norby, *Am. J. Med.*, 2000, **109**, 665–678.
28 H. Wei, D. Jiang, B. Yu, D. Ni, M. Li, Y. Long, P. A. Ellison, C. M. Siamof, L. Cheng, T. E. Barnhart, H.-J. Im, F. Yu, X. Lan, X. Zhu, Q. He and W. Cai, *Bioact. Mater.*, 2023, **19**, 282–291.
29 R. Bellomo, J. A. Kellum and C. Ronco, *Lancet*, 2012, **380**, 756–766.
30 N. A. Hukriede, D. E. Soranno, V. Sander, T. Perreau, M. C. Starr, P. S. T. Yuen, L. J. Siskind, M. P. Hutchens, A. J. Davidson, D. M. Burmeister, S. Faubel and M. P. de Caestecker, *Nat. Rev. Nephrol.*, 2022, **18**, 277–293.
31 N. M. Selby and J. Duranteau, *Curr. Opin. Crit. Care*, 2020, **26**, 543–548.
32 C. Wang, C. Gao, W. Maimaiti, S. Li, Q. Yang and L. Jiang, *PLoS One*, 2020, **15**, e0237443.
33 B. Yang, Y. Chen and J. Shi, *Chem. Rev.*, 2019, **119**, 4881–4985.
34 C. Li, Y. Xue, X. Ba and R. Wang, *Cells*, 2022, **11**, 3798.
35 C. J. Burrows and J. G. Muller, *Chem. Rev.*, 1998, **98**, 1109–1152.
36 D. Liu, G. Shu, F. Jin, J. Qi, X. Xu, Y. Du, H. Yu, J. Wang, M. Sun, Y. You, M. Zhu, M. Chen, L. Zhu, Q. Shen, X. Ying, X. Lou, S. Jiang and Y. Du, *Sci. Adv.*, 2020, **6**, eabb7422.
37 X. Yu, X. Chi, S. Wu, Y. Jin, H. Yao, Y. Wang, Z. Xia and J. Cai, *Oxid. Med. Cell. Longevity*, 2016, **2016**, 4675817.
38 X. Zhao, L.-Y. Wang, J.-M. Li, L.-M. Peng, C.-Y. Tang, X.-J. Zha, K. Ke, M.-B. Yang, B.-H. Su and W. Yang, *Adv. Sci.*, 2021, **8**, e2101498.
39 D. Ni, D. Jiang, C. J. Kutyreff, J. Lai, Y. Yan, T. E. Barnhart, B. Yu, H.-J. Im, L. Kang, S. Y. Cho, Z. Liu, P. Huang, J. W. Engle and W. Cai, *Nat. Commun.*, 2018, **9**, 5421.
40 Q. Chen, Y. Nan, Y. Yang, Z. Xiao, M. Liu, J. Huang, Y. Xiang, X. Long, T. Zhao, X. Wang, Q. Huang and K. Ai, *Bioact. Mater.*, 2023, **22**, 141–167.